

Mesh Denoising Transformer

Wenbo Zhao, *Member, IEEE*, Xianming Liu, *Member, IEEE*, Deming Zhai, *Member, IEEE*, Junjun Jiang, *Member, IEEE*, and Xiangyang Ji, *Member, IEEE*

Abstract—Mesh denoising, aimed at removing noise from input meshes while preserving their feature structures, is a practical yet challenging task. Despite the remarkable progress in learning-based mesh denoising methodologies in recent years, their network designs often encounter two principal drawbacks: a dependence on single-modal geometric representations, which fall short in capturing the multifaceted attributes of meshes, and a lack of effective global feature aggregation, hindering their ability to fully understand the mesh’s comprehensive structure. To tackle these issues, we propose *SurfaceFormer*, a pioneering Transformer-based mesh denoising framework. Our first contribution is the development of a new representation known as *Local Surface Descriptor*, which is crafted by establishing polar systems on each mesh face, followed by sampling points from adjacent surfaces using geodesics. The normals of these points are organized into 2D patches, mimicking images to capture local geometric intricacies, whereas the poles and vertex coordinates are consolidated into a point cloud to embody spatial information. This advancement surmounts the hurdles posed by the irregular and non-Euclidean characteristics of mesh data, facilitating a smooth integration with Transformer architecture. Next, we propose a dual-stream structure consisting of a *Geometric Encoder* branch and a *Spatial Encoder* branch, which jointly encode local geometry details and spatial information to fully explore multimodal information for mesh denoising. A subsequent *Denoising Transformer* module receives the multimodal information and achieves efficient global feature aggregation through self-attention operators. Our experimental evaluations demonstrate that this novel approach outperforms existing state-of-the-art methods in both objective and subjective assessments, marking a significant leap forward in the field of mesh denoising.

Index Terms—mesh denoising, transformer, surface descriptor, multimodal.



1 INTRODUCTION

MESHES play an integral role in the domain of computer graphics and geometric processing, serving as the backbone for 3D shape representation, manipulation, and visualization. Their applications span a wide range of fields, including but not limited to 3D printing [1], medical imaging [2], and augmented reality [3], enabling the detailed and flexible modeling of intricate geometries. The critical role of meshes in these applications underscores the importance of maintaining high-quality mesh data. However, meshes are prone to noise, which can stem from various sources such as the acquisition process (e.g., through 3D scanning) or subsequent processing stages, leading to a degradation in quality. This challenge has catalyzed significant research in the area of mesh denoising, which aims to eliminate noise while preserving vital geometric features like edges and corners.

Mesh denoising represents a complex and challenging ill-posed problem, aiming to smooth noisy surfaces while preserving the original features of the object and preventing unnatural geometric distortions. At the early stage, mesh denoising strategies were inspired by image denoising techniques, utilizing methods based on filtering [4], [5] or optimization [6], [7]. However, the unique attributes of mesh data, such as shape and topological relationships, make image-specific algorithms less effective for this task. As a result, these strategies often depend on low-dimensional

geometric representations to simplify algorithm implementation and introduce additional prior knowledge about the shape or noise to aid in denoising. For instance, filtering-based approaches [8], [9], [10] typically utilize face normals and center distances as geometric representations, leveraging these to determine filtering weights. Meanwhile, optimization-based approaches [11], [12], [13] generally assume Gaussian-distributed noise and incorporate shape priors like piecewise-smooth constraints. These methods prove effective for CAD-like models, which are characterized by structured shapes and planar surfaces. However, they often struggle with complex or scanned models, leading to over-smoothing or the introduction of pseudo features due to the loss of mesh attributes and the limited generalization capability of the algorithms.

The advent of deep neural networks (DNNs) has significantly advanced data-driven mesh denoising [14], [15], [16]. DNNs are capable of directly mapping high-dimensional inputs to their ground truth, eliminating the need for complex inputs and additional prior knowledge. This has shifted the focus towards developing geometric representations that encapsulate more mesh attributes and network architectures with enhanced denoising capabilities. Early studies [14], [17] employed filtering-based normal representation and utilized multilayer perceptron (MLP) networks for denoising. However, the limited expressive power of these representations and MLP’s generalization capacity impacted denoising outcomes. Researchers have since explored more powerful architectures, divided into two categories: 1) some works attempted to create regular geometric representations, such as non-local normal matrices [18] or voxel representations [15], so as to leverage convolutional neural networks (CNNs) based networks; 2) others advocated for constructing graphs

- W. Zhao, X. Liu, D. Zhai, J. Jiang are with the Faculty of Computing, Harbin Institute of Technology, Harbin, China, 150001. E-mail: {cxsm,zhaideming,jiangjun}@hit.edu.cn
- X. Ji is with the Department of Automation, Tsinghua University, Beijing 100084, China. E-mail: xyji@tsinghua.edu.cn.

based on the topological structure of the mesh and preserving geometry information through node embedding, leading to the widespread adoption of graph neural networks (GNNs) [16], [19], [20]. These approaches achieve superior denoising performance compared to traditional methods.

Despite these advancements, existing learning-based approaches still fall short in achieving satisfactory feature recovery results, which is attributed to two main factors. The first issue lies in the limitations of their network architectures, which are often confined to single-modal geometric representations. Such representations are insufficient for capturing the complex attributes of meshes, leading to a significant loss of attributes during the construction of representations. For instance, CNN-based methods, such as those discussed in [15], [18], struggle to process the irregular spatial information inherent in meshes, whereas GNN-based methods [16], [19], [20], encounter difficulties in embedding detailed geometric information, resulting in the loss of geometric details. The second challenge is the networks' limited capability to capture global features. Typically, these networks attempt to accumulate global information through the stacking of convolutional layers or aggregations of graph nodes. However, the localized receptive fields of these layers are inadequate for managing long-range dependencies and understanding the overall structure of the mesh. This limitation hampers their ability to restore large-scale features that necessitate a comprehensive grasp of global structural information.

To overcome the above challenges, the exploration of advanced neural network architectures such as the Transformer [21] for mesh denoising presents a promising avenue, due to the Transformer's ability to manage long-range dependencies and its flexibility in handling complex data structures. The Transformer's architecture, characterized by self-attention mechanisms, enables it to focus on relevant parts of the data regardless of their position, making it well-suited for tasks requiring an understanding of global context and structural relationships [22]. This feature is particularly relevant for mesh denoising, where capturing the global geometric structure and the intricate relationships between different parts of the mesh is crucial for effective denoising while preserving essential features. Despite the potential advantages, the adoption of Transformer models for mesh denoising has been relatively slow, with a notable absence of research in this area. One of the primary reasons for this slow adoption is the challenge of data representation. The irregular and non-Euclidean characteristics of mesh data present substantial hurdles in formulating a representation that is compatible with Transformer models. Unlike images or sequences, which have regular and structured data formats, meshes require specialized representations that can effectively capture their geometric and topological properties.

Recent research in mesh-related tasks, such as mesh classification and segmentation [23], mesh understanding [24], human pose and mesh reconstruction [25], [26], [27], has explored to incorporate the Transformer architecture. These initiatives employed various encoders to handle multi-modal geometric representations and aggregate global information through the self-attention operator. Despite these advancements, current Transformer-based approaches in mesh

processing often rely on existing representations like point clouds [23] or heat maps [27], which may result in attribute loss. Furthermore, these networks are primarily designed for tasks of mesh understanding [23], [24] or 3D human pose and mesh reconstruction [25], [26], [27], which are not directly applicable to mesh denoising without significant modifications.

In this study, we introduce a novel geometric representation called *Local Surface Descriptors* (LSDs) to bridge this gap. LSDs are generated by setting up polar systems on each mesh face, from which points on adjacent surfaces are sampled using geodesic rays. The normals of these points are then arranged into 2D patches resembling images to capture local geometric details, while the poles are treated as a point cloud to encapsulate spatial information. This innovation overcomes the challenge posed by the irregular and non-Euclidean nature of mesh data, enabling seamless integration with Transformer models. We further present *SurfaceFormer*, a powerful Transformer-based mesh denoising approach that employs a dual-stream structure to process multi-modal geometric representations and harnesses the Transformer architecture's superior global feature aggregation capabilities. Inspired by the success of Transformers in multi-modal tasks, *SurfaceFormer* includes a Geometric Encoder branch and a Spatial Encoder branch to process local geometric and spatial information, respectively, converging in a Denoising Transformer module designed for effective feature aggregation. Our experimental evaluations demonstrate that *SurfaceFormer* outperforms existing state-of-the-art mesh denoising methods, marking a significant leap forward in the field.

The primary contributions of this work are highlighted as follows:

- We introduce *SurfaceFormer*, a pioneering Transformer-based mesh denoising framework that innovatively achieves multimodal geometric representation and global feature aggregation. This is, to the best of our knowledge, the first instance of applying Transformer architecture within the mesh denoising domain.
- We propose a novel representation called *Local Surface Descriptors*, which efficiently preserves both the local geometry details and spatial information in a unified format, enabling smooth integration with Transformer architecture.
- We offer extensive experimental results to demonstrate that *SurfaceFormer* achieves substantial enhancements over current state-of-the-art methods in both subjective and objective evaluations, thanks to innovative network structures and geometric representations.

This paper significantly extends our preliminary work [28], with notable advancements. Firstly, we refine the network architecture by integrating Transformers and introducing self-attention mechanisms. This development considerably boosts the network's ability to extract and synthesize features, addressing previously identified denoising limitations. Secondly, the representation design is optimized by incorporating multimodal geometric representations, which effectively retain both local geometric and spatial infor-

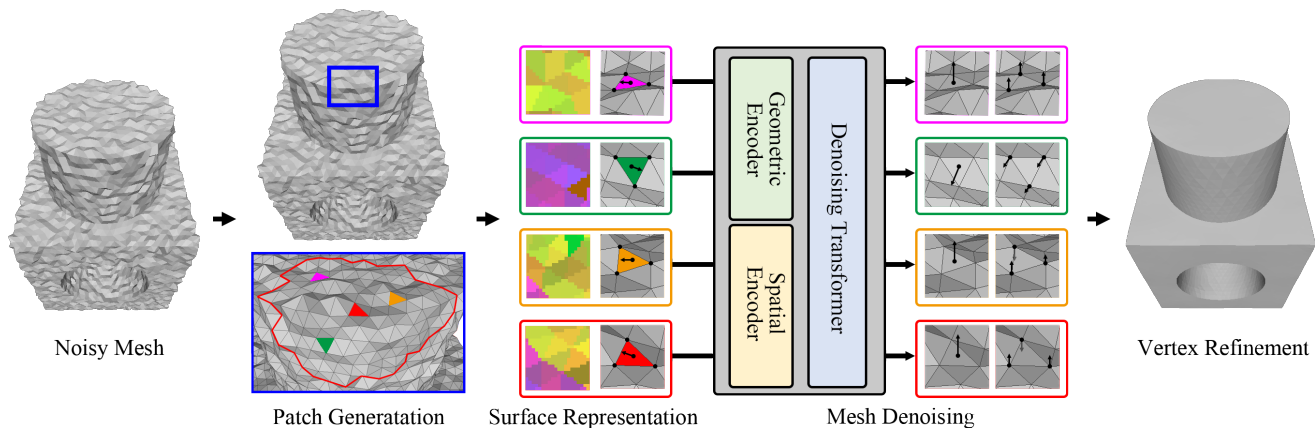


Fig. 1. The overall framework of the proposed method, which includes four main steps: **Patch Generation**, **Surface Representation**, **Mesh Denoising** and **Vertex Refinement**.

mation. This approach successfully mitigates the feature loss issue seen with single-modal representations in our initial version. Furthermore, we perform an extensive experimental analysis against the latest state-of-the-art methods, showcasing the superior performance and effectiveness of our approach.

The remainder of this paper is structured as follows: Section 2 offers a concise overview of related works. The methodology behind *SurfaceFormer* is detailed in Section 3. Experimental results are discussed in Section 4, and Section 5 provides the conclusion of the paper.

2 RELATED WORKS

In this section, we review the related works from three aspects, including traditional approaches, data-driven approaches and GNN-based approaches

2.1 Traditional Approaches

Traditional approaches to mesh denoising have largely been developed from image denoising techniques, including filtering and optimization approaches. Early technologies typically utilized a one-stage framework that directly applies these techniques to noisy vertex positions. For instance, Fleishman *et al.* [29] and Jones *et al.* [30] employed bilateral filter for feature-preserving denoising. Clarenz *et al.* [31], [32], [33] adapted the anisotropic diffusion filtering for mesh denoising. He *et al.* [11] introduced L_0 minimization for mesh denoising, leveraging differential edge operator and triangle shape regularization as optimization terms. Wu *et al.* [12] introduced L_1 minimization, incorporating vertex fidelity, total variation-based edge and triangle shape regularization. However, subsequent studies [8], [9] indicated that face normals offer a more accurate representation of local surface geometry than vertex positions. Consequently, the two-stage framework has gained popularity, which firstly denoises the face normals and then update the vertex positions according to the denoised normals. For instance, Zheng *et al.* [8] applied bilateral filter to face normals, determining filtering weights by center and normal distances. Zhang *et al.* [9] introduced guided filter for mesh denoising, utilizing the average normal of the most consistent 1-ring

sub-patch as guidance normals. Zhao *et al.* [34] proposed to use graph cuts to obtain feature-aware sub-patches for computing guidance normals. Recent efforts have sought to incorporate non-local information. This includes strategies such as adding non-local normals from similar patches during filtering [35] and organizing normals from similar patches into matrices, followed by low-rank recovery [36].

Nevertheless, these methods generally require specific prior knowledge, such as the Gaussian noise distribution or piecewise-smooth shape prior. Consequently, these methods are only effective for CAD-like models that with simple structure, when facing complex or scanned models, they fail to produce satisfactory results, often leading to over-smoothing or introducing pseudo-features.

2.2 Data-driven approaches

To address the aforementioned problems, researchers have embarked on exploring data-driven algorithms that directly learn the mapping from noisy data to ground truth. However, neural networks typically require regular input, and the irregular structure of mesh prevents the implement of neural networks. To tackle this problem, researchers have proposed a variety of geometric representations to convert irregular mesh information into regular structures. For instance, Wang *et al.* [14] proposed to iteratively apply bilateral or guided filter on noisy meshes, the filtered normals are then organized as the filtered facet normal descriptor, and fed to MLP to obtain denoised normals. Wei *et al.* [37] and Wang *et al.* [17] improved this method by introducing generalized reverse descriptor and low-rank matrix recovery based preprocess. Nevertheless, the limited ability of descriptors to preserve features hinders the performance of these algorithms. To tackle this challenge, researchers have explored the construction of more efficient geometric representations. Li *et al.* [38] represent local topological information as adjacency matrices, and use cascaded residual units to predict the denoised normals. Li *et al.* [18] searched similar patches on the whole meshes to explore non-local information, and organized their normals to matrix, which allows the implement of CNN. Zhu *et al.* [39] built 2D height map to present the local geometric information. Zhao *et al.* [15] introduce voxelization to roughly represent the local shape information, and employ 3D Resnet for denoising.

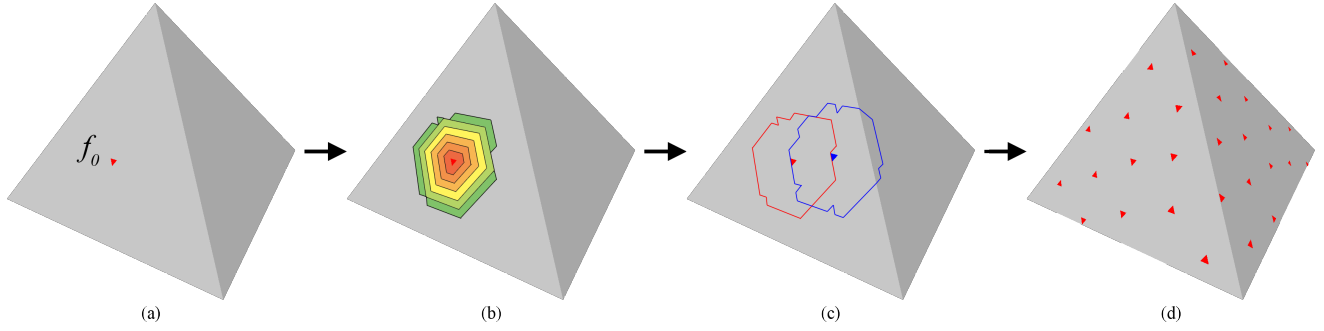


Fig. 2. The patch generation process of *Pyramid* when $T_f = 240$. (a) f_0 is employed as the initial patch center, highlighted in red. (b) K-ring faces surrounding f_0 are incorporated into the patch until the number of faces reaches T_f . (c) The nearest unvisited face to f_0 becomes the next center, highlighted in blue. Another patch is built around it. (d) This procedure continues until all the faces are visited, and the patch centers are highlighted in red.

These methods have made significant progress in preserving geometric information. However, the spatial information of mesh is difficult to be converted into a regular form, and is therefore usually discarded, which reduces the ability of the algorithm to distinguish feature structures.

2.3 GNN based Approaches

Since meshes inherently possess a graph structure defined by vertex and face connectivity, prompting researchers to leverage graph neural networks (GNNs) for enhancing spatial information preservation. Armando *et al.* [19] pioneered GNN-based method for face normal denoising by treating each face as a node and building edges between adjacent faces. Shen *et al.* [16] employed static and dynamic graph convolutions to connect non-adjacent graph nodes. Zhang *et al.* [20] proposed building graphs on both faces and vertices, enabling simultaneous denoising in normal and vertex domains, followed by a vertex refinement strategy to align denoised normals and vertex coordinates. Hattori *et al.* [40] also constructed two graphs and introduced self priors, such as smoothness error and normal consistency, to achieve self-supervised mesh denoising. Recently, Tang *et al.* proposed DOGNET [41] consisting of cascaded networks that conduct localized graph neural network operations to aggregate features from neighborhoods, and iteratively propagate information across the mesh. Zhao *et al.* [42], [43] further introduced curvature domain denoising to improve the feature preserving denoising performance. Zhou *et al.* [44] proposed predicting vertex offsets instead of directly predicting positions, facilitating network convergence and yielding improved results.

While GNNs offer significant advantages over traditional neural networks in preserving spatial information, they often lack the design of geometric attribute embeddings, resulting in the loss of local geometric information and thereby limiting method performance.

3 METHODOLOGY

3.1 Overview

Define $\mathcal{X} = \{\mathcal{V}, \mathcal{F}\}$ as the input noisy mesh, where $\mathcal{V} = \{v_i\}$ and $\mathcal{F} = \{f_i\}$ denote the sets of vertices and faces, respectively. Our objective is to perform denoising in both normal and vertex domains, followed by aligning the

denoised vertex coordinates and face normals to generate the denoised mesh $\hat{\mathcal{X}}$. As illustrated in Fig. 1, the proposed *SurfaceFormer* encompasses four principal phases:

- **Patch Generation.** This phase involves the segmentation of the input noise mesh \mathcal{X} into equally-sized patches. By dividing the mesh into smaller, manageable patches, it allows for more focused and efficient processing of local geometries. The segmentation is designed to ensure that each patch contains a portion of the mesh that is sufficiently representative of the local structure, allowing for accurate local surface reconstruction in later phases.
- **Surface Representation.** In this phase, each segmented patch is encoded using the Local Surface Descriptor (LSD), which captures the mesh’s local geometric details as well as spatial information. The geometric details are represented in the form of image-like 2D matrices, while the spatial information is captured as a point cloud. This dual representation is critical for preserving the intricate details of the mesh’s surface, ensuring that the model has access to comprehensive information about the local geometry of each patch.
- **Mesh Denoising.** Upon representing the surface of each patch, the *SurfaceFormer* processes the LSD to mesh denoising. The process involves two main steps: the 2D matrices are fed into a Geometric encoder, and the point cloud into a Spatial encoder. These encoders extract and refine features from their respective inputs, which are then fused together. The fused features undergo further refinement in the Denoising Transformer, which accurately reconstructs the surface normals and vertex coordinates.
- **Vertex Refinement.** While denoised meshes can be obtained by using only denoised surface normals or vertex coordinates, this may introduce artificial effects to mesh and reduce surface consistency, respectively. Therefore, an iterative refinement strategy is employed to align denoised vertex coordinates with face normals to further refine the denoising results and output the final denoised meshes.

By addressing both geometric and spatial aspects of the mesh and leveraging advanced encoding and transformation techniques, *SurfaceFormer* promises enhanced accuracy

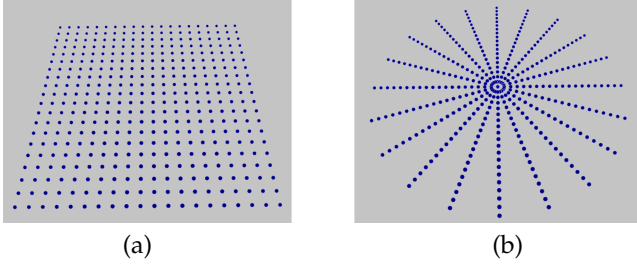


Fig. 3. Sample 20×20 points (a) with uniformly distributed Cartesian coordinates, in which the sampling density is consistent. (b) with uniformly distributed polar coordinates, in which the sampling density tends to be sparser with increased radius.

and detail preservation in the denoised mesh output. In the following, we will introduce the four phases in details.

3.2 Patch Generation

Given the extensive variety of mesh sizes, which can encompass up to millions of faces, the task of directly denoising an entire mesh proves to be too demanding for standard GPUs due to the substantial computational resources required. To circumvent this limitation, we employ a segmentation strategy inspired by Transformer-based methods for processing lengthy inputs [45], [46]. This strategy involves dividing noisy meshes into overlapping patches. As demonstrated in Fig. 2, we commence by selecting a face to serve as the center of a patch. For the sake of simplicity, the first face f_0 is chosen as this center. Following this, we progressively incorporate the k -ring neighbors of f_0 into the patch, continuing this process until the number of faces in the patch reaches a predetermined limit T_f . Subsequently, we identify the closest unvisited face to f_0 to serve as the center for the next patch, and this process is repeated, allowing us to construct patches until every face has been accounted for.

An important consideration of this segmentation approach is that it results in each face undergoing the denoising process multiple times, which in turn produces several denoised normals and vertex coordinates for each face. The approach to resolving this issue is further elaborated in the *Vertex Refinement* section.

3.3 Surface Representation

We then delve into the detailed process of generating the LSD. Given a patch $P = \{f_i\}$, the goal of LSD is to convert the mesh attributes of each face in P into two components with different modal: an image-like matrix \mathbf{g} that captures local geometric details, and a featured point \mathbf{s} that represents the spatial information. Specifically, for a face f_i , we uniformly sample a set of points $\{p_{(i,j)}\}$, $i, j \in (-T_s, T_s]$ around a chosen pole, where T_s is a parameter determining the number of sampling points. The normals of these sampled points and the pole are then compiled into the LSD $(\mathbf{g}_i, \mathbf{s}_i)$ of f_i . Finally, these LSDs are aggregated into a matrix sequence $\mathbf{G} = \{\mathbf{g}_i\}$ and a point cloud $\mathbf{S} = \{\mathbf{s}_i\}$, which serve as the input to the denoising network.

3.3.1 Generation of LSD

Addressing the complex challenge of achieving uniform sampling on the curved surfaces of meshes is pivotal for

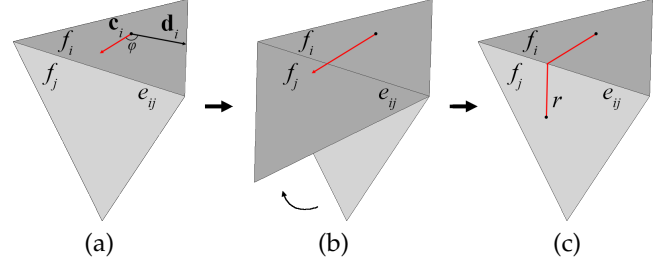


Fig. 4. An example of sampling by shooting geodesic. The polar coordinate system is built on f_i , \mathbf{c}_i and \mathbf{d}_i are the polar and axis, respectively. (a) The geodesics starts from \mathbf{c}_i at angle φ . (b) When the geodesics reaches edge e_{ij} , f_j is rotated to the same plane as f_i around e_{ij} to allow the propagation. (c) The geodesics stops propagation when the length is equal to r , and the end point is regarded as the sampling point.

generating LSD. While uniform sampling on planar surfaces can be straightforwardly achieved by setting up a 2D Cartesian coordinate system and methodically choosing a set of Cartesian coordinates, as depicted in Fig.3-(a), this approach falls short when applied to curved surfaces.

Previous studies, such as [47], introduced the use of a polar coordinate system $\{p_s\} = \{r, \varphi\}$ on mesh surfaces, where r represents the radial distance and φ the angular direction. In this method, geodesics are projected from a central point to divide the local surface into several sectors, gathering data within each sector to create a shape context descriptor. Drawing inspiration from this technique, we devise a sampling methodology that projects geodesics at specific polar coordinates and utilizes the endpoints as the sampling points. As illustrated in Fig. 4, considering a current face f_i , its neighboring face f_j , and their connecting edge e_{ij} , we use the center \mathbf{c}_i of f_i as the pole and a ray \mathbf{d}_i from \mathbf{c}_i to the midpoint of one of f_i 's edges as the axis. A geodesic is initiated from \mathbf{c}_i at a specific angle φ and, upon reaching e_{ij} , the adjoining face f_j is aligned onto the same plane as f_i by rotation around e_{ij} , facilitating the geodesic's continuation on this plane. This process repeats until the geodesic attains a total length of r , with the endpoint serving as the sampling point.

Nevertheless, achieving uniform sampling remains a challenging task due to the fact that the sampling density gradually decreases with increasing r , as shown in Fig. 3-(b). To overcome this problem, we propose a coordinate transformation strategy that leverages the benefits of both Cartesian and polar coordinate systems. Specifically, our goal is to generate a polar coordinate set $\{(r_{(i,j)}, \varphi_{(i,j)})\}$, $i, j \in (-T_s, T_s]$ using the coordinate transformation strategy. Initially, a virtual Cartesian system $\{c_s\} = \{vx, vy\}$ is established. A virtual coordinate set $\{(vx_i, vy_j)\}$ with square distribution is then generated in the system. To adapt the distance between sampling points to the mesh scale, the virtual Cartesian coordinates are calculated by:

$$(vx_i, vy_j) = \left(\frac{d_a}{p_s} i, \frac{d_a}{p_s} j \right) \quad (1)$$

where d_a represents the average Euclidean distance between adjacent face centers in the noisy mesh, serving as a scale estimate; p_s is the parameter controlling sampling precision. Subsequently, the virtual Cartesian coordinates (vx_i, vy_j)

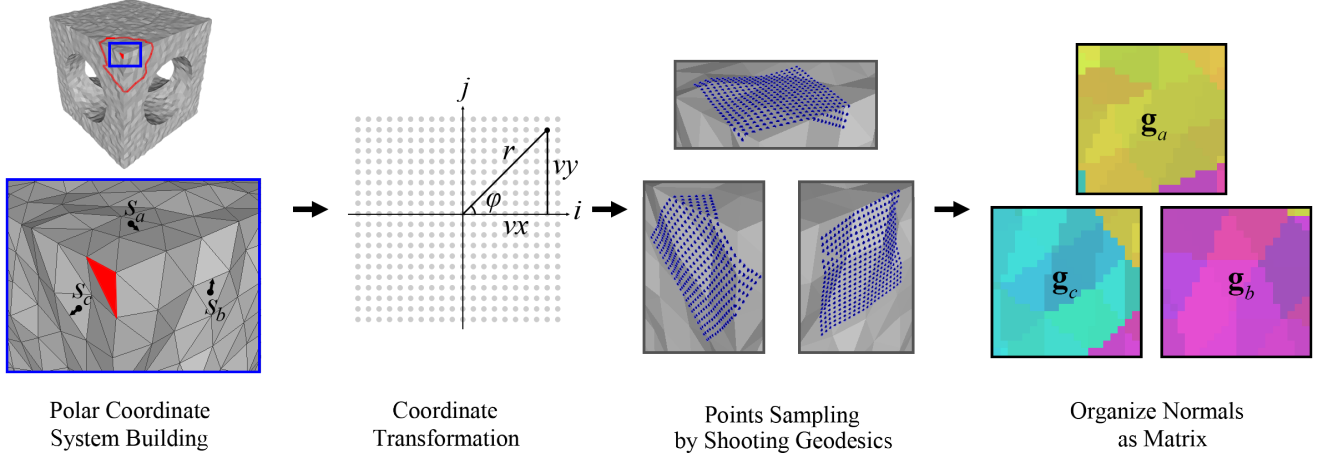


Fig. 5. An illustration of the LSD generation with $T_s = 10$.

are transformed into polar coordinates $(r_{(i,j)}, \varphi_{(i,j)})$:

$$r_{(i,j)} = \sqrt{(vx_i)^2 + (vy_j)^2}, \varphi_{(i,j)} = \arctan \frac{vy_j}{vx_i} \quad (2)$$

After obtain the polar coordinate set, we adopt the sampling strategy to obtain regular sampling points, and their normals $\{\mathbf{n}_{(i,j)}\}$ of the sampling points are arranged into a matrix as \mathbf{g}_i . We also preserve the pole and the three vertex coordinates of f_i as the spatial information $\mathbf{s}_i = [\mathbf{c}_i, \mathbf{d}_i, \mathbf{v}_i^1, \mathbf{v}_i^2, \mathbf{v}_i^3]$, where $\mathbf{v}_i^1, \mathbf{v}_i^2, \mathbf{v}_i^3$ denotes the vertices of f_i . Finally, we consolidate the LSDs of all the faces in P to a matrix sequence $\mathbf{G} \in \mathbb{R}^{T_f \times ((2T_s)^2 \times 3)}$ and a point cloud $\mathbf{S} \in \mathbb{R}^{T_f \times 15}$.

For better understanding, we present the LSD generation of three different faces in Fig. 5, which presents the LSDs of three distinct faces. It reveals that the proposed strategy ensures that the sampling points are uniformly distributed on the surface of the object, and the normals of sampling points can accurately capture the feature structures around each face.

3.3.2 Normalization

We further implement a normalization strategy to ensure that the LSDs possess scale and rotation invariance. Specifically, we translates the patch center to the origin, and scale the patch to fit within $[-1, 1]$. Then we calculate the average normal $\bar{\mathbf{n}}$ of the faces in P , and utilize Rodrigues' rotation formula [48] to derive the rotation matrix that aligns $\bar{\mathbf{n}}$ with a predetermined direction \mathbf{n}_t :

$$\theta = \angle(\bar{\mathbf{n}}, \mathbf{n}_t), \mathcal{R} = \mathbf{I} + (\sin\theta) \mathbf{N} + (1 - \cos\theta) \mathbf{N}^2 \quad (3)$$

where \mathbf{N} is the skew-symmetric cross-product matrix of $\bar{\mathbf{n}} \times \mathbf{n}_t$.

The translation and rotation are then applied on the LSDs to get normalized $\tilde{\mathbf{G}}$ and $\tilde{\mathbf{S}}$:

$$\begin{aligned} \tilde{\mathbf{n}}_{(i,j)} &= \mathcal{R} \mathbf{n}_{(i,j)}, \tilde{\mathbf{d}}_i = \mathcal{R} \mathbf{d}_i, \\ \tilde{\mathbf{c}}_i &= \frac{\mathcal{R}(\mathbf{c}_i - \mathbf{c}_0)}{M_v}, \tilde{\mathbf{v}}_i = \frac{\mathcal{R}(\mathbf{v}_i - \mathbf{c}_0)}{M_v} \end{aligned} \quad (4)$$

where \mathbf{c}_0 denotes the center of the patch center face, M_v denotes the the maximum absolute value of all the coordinate components.

It is critical to note that the denoised normals and vertices derived from the normalized LSDs are also normalized. Therefore, we also calculate the inverse rotation matrix \mathcal{R}^{-1} and keep \mathbf{c}_0, M_v to facilitate the reversion of results after denoising.

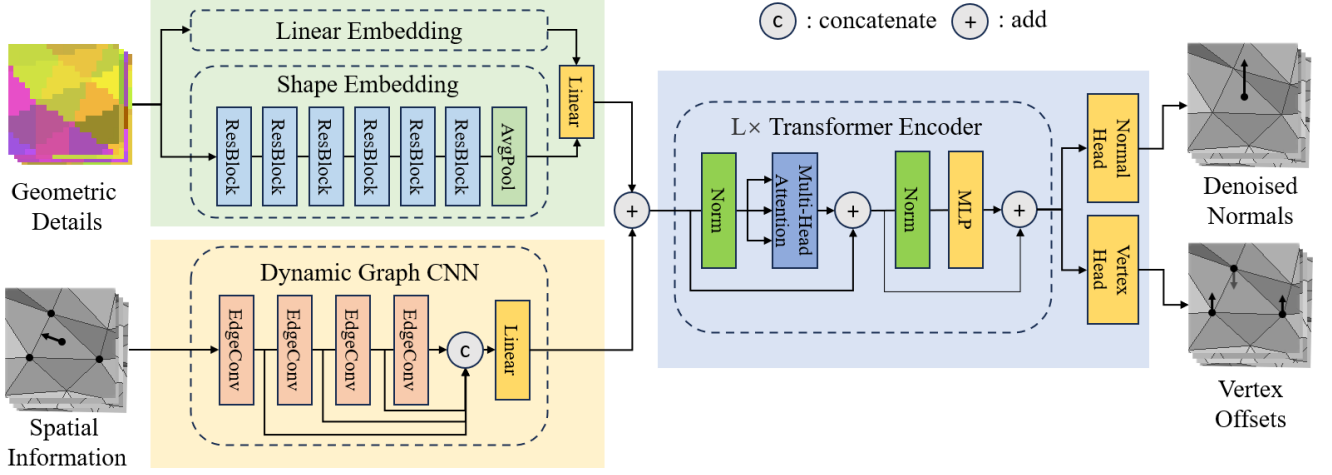
3.4 Mesh Denoising

The proposed LSD preserves both geometric and spatial information, which allows us to follow the multi-domain mesh denoising approaches [20], [43], [44], achieving normal and vertex denoising simultaneously. Specifically, the normalized LSDs are fed to the proposed *SurfaceFormer* to predict the denoised face normals $\{\hat{\mathbf{n}}_i\}$ and vertex coordinate offsets $\{\Delta \hat{\mathbf{v}}_i\}$, which features a dual-stream structure, comprising a Geometric Encoder branch and a Spatial Encoder branch, culminating in a Denoising Transformer. As illustrated in Fig. 6, the Geometric Encoder and Spatial Encoder collaboratively process $\tilde{\mathbf{G}}$ and $\tilde{\mathbf{S}}$, respectively, projecting them into \mathbf{F}_g and \mathbf{F}_s as geometric and spatial features. These features are then fed into the Denoising Transformer to achieve global feature aggregation and denoising. The functionality and details of these three key components will be elaborated upon in the subsequent subsections.

3.4.1 Geometric Encoder

Leveraging the similarity between the matrix sequence $\tilde{\mathbf{G}}$ and image patches in Visual Transformer (ViT) [49], employing the linear embedding from ViT has demonstrated effective denoising outcomes. However, it is crucial to recognize that $\tilde{\mathbf{G}}$ embodies the mesh's piecewise-smooth nature, in which the edges of faces play an important role in reflecting the shape information and feature structures. Linear embedding could potentially reduce the correlation among edges, resulting in the loss of feature details. To address this issue, as highlighted in the green box in Fig. 6, the proposed Geometric Encoder incorporates both linear embedding and shape embedding for capturing normal and edge information, respectively. Given the input $\tilde{\mathbf{G}}$, the output \mathbf{F}_g is generated as below:

$$\mathbf{F}_g = L_m \left(\left[E_L \left(\tilde{\mathbf{G}} \right), E_C \left(\tilde{\mathbf{G}} \right) \right] \right), \mathbf{F}_g \in \mathbb{R}^{T_f \times D} \quad (5)$$


 Fig. 6. The network architecture of *SurfaceFormer*.

where E_L represents the linear embedding from ViT [49], E_C represents the shape embedding, which is a lightweight ResNet [50] that consist of 6 ResNet Blocks and an average pooling, each block featuring two 3×3 convolution layers with residual connections linking the input and output of each block, the channel number of all the convolution layers is 32. L_m denotes a linear projection that fuses the outcomes of both embeddings, producing a D -dimensional geometric feature \mathbf{F}_g . The Spatial Encoder serves a similar purpose to positional Embedding in Transformer architecture, equipping the network with the capability to recognize and leverage positional correlations. However, due to the variable nature of positional relationships in point clouds, employing a pre-trained weight matrix, as done in image or natural language processing domains [21], [51], is unfeasible. To address this challenge, we utilize the Dynamic Graph CNN [52] as a trainable Spatial Encoder E_S to capture local geometric details. Following the configuration in [52], our Spatial Encoder includes four EdgeConv operations designed to extract features across multiple scales, whose output dimension are 64, 64, 128 and 256, respectively. These extracted features are subsequently concatenated and processed through a linear layer to produce the spatial feature \mathbf{F}_s , defined as follows:

$$\mathbf{F}_g = E_S(\tilde{\mathbf{S}}), \mathbf{F}_g \in \mathbb{R}^{T_f \times D} \quad (6)$$

For the ease of feature fusion later in the process, we ensure that the dimensions of \mathbf{F}_s match those of \mathbf{F}_g .

3.4.2 Denoising Transformer

The initial step involves combining the geometric and spatial features to obtain the fused feature. We adopt the design of ViT [49] that achieves fusion through addition:

$$\mathbf{F}_0 = \mathbf{F}_g + \mathbf{F}_s, \mathbf{F}_0 \in \mathbb{R}^{T_f \times D} \quad (7)$$

Subsequently, we utilize $L \times$ Transformer Encoders to facilitate global feature aggregation. These encoders comprise multi-head self-attention (MSA) and multilayer perceptrons (MLP), both augmented with Layer Normalization (LN) and residual connections. All the encoders maintains a constant

latent feature with size D and employ N_h attention heads. The feature aggregation process is defined as follows:

$$\mathbf{F}'_i = \text{MSA}(\text{LN}(\mathbf{F}_{i-1})) + \mathbf{F}_{i-1}, i \in [1, L] \quad (8)$$

$$\mathbf{F}_i = \text{MLP}(\text{LN}(\mathbf{F}'_i)) + \mathbf{F}'_i, i \in [1, L] \quad (9)$$

The output \mathbf{F}_L is then directed to the normal head H_n and vertex head H_v to produce the normalized denoised normal $\{\hat{\mathbf{n}}_i\}$ and three vertex coordinate offsets $\{\Delta\hat{\mathbf{v}}_i\}$ of each face. For vertex denoising, we apply a linear layer with LN to yield 9-dimensional output values, formulated as:

$$\{\Delta\tilde{\mathbf{v}}_i\} = H_v(\text{LN}(\mathbf{F}_L)) \quad (10)$$

It is important to note that each vertex may belong to multiple faces, which also yields duplicate denoising results and will be resolved in *Vertex Refinement* section.

For normal denoising, given that $\{\hat{\mathbf{n}}_i\}$ are expected to be unit vectors, we apply a linear layer with LN and normalization (NL) to yield 3-dimensional output values H_n , formulated as:

$$\{\hat{\mathbf{n}}_i\} = \text{NL}(H_n(\text{LN}(\mathbf{F}_L))) \quad (11)$$

Finally, we apply the inverse rotation and transformation to recover the denoised normals and vertices:

$$\{\hat{\mathbf{n}}_i\} = \mathcal{R}^{-1}\{\tilde{\mathbf{n}}_i\}, \{\hat{\mathbf{v}}_i\} = M_v\mathcal{R}^{-1}(\{\mathbf{v}_i + \Delta\hat{\mathbf{v}}_i\} + \mathbf{c}_0) \quad (12)$$

3.5 Vertex Refinement

The proposed *Patch Generation* and *Mesh Denoising* strategy will produce multiple denoised normals and vertex coordinates for each face. To address this problem, we straightforwardly employ the average denoised normals $\bar{\mathbf{n}}_i$ and $\bar{\mathbf{v}}_i$ as the denoised results.

Upon obtaining the denoised normals and vertex coordinates, two common methods can be employed to obtain the final denoised mesh: updating vertex coordinates based on denoised normals [9] or directly utilizing denoised vertex coordinates [29]. However, since existing vertex updating methods [9] fail to capture the underlying patterns of vertex

distribution, the first method may introduce artificial effects to the denoised mesh. The second method can avoid this issue, but the denoised vertex coordinates demonstrate less local consistency than surface normals, resulting in the inability to produce smooth denoising results. To address this challenge, we employ the vertex refinement scheme [20] which aligns the denoised vertex coordinates with face normals, thereby resolving the aforementioned problems:

$$\bar{\mathbf{v}}_i' = \bar{\mathbf{v}}_i + \frac{1}{|\theta_{\mathbf{v}}|} \sum_{f_i \in \theta_{\mathbf{v}}} \bar{\mathbf{n}}_i (\bar{\mathbf{n}}_i \cdot (\mathbf{c}_i - \bar{\mathbf{v}}_i)) \quad (13)$$

where $\theta_{\mathbf{v}}$ denotes the set of faces that include vertex \mathbf{v} . This refinement process is repeated for N_v times and outputs the final denoised mesh $\hat{\mathcal{X}}$.

4 NETWORK TRAINING

The training set of *SurfaceFormer* is constructed from a set of noisy meshes $\{\mathcal{X}\}$ and their corresponding noise-free meshes $\{\mathcal{X}^*\}$. Specifically, we build a patch around each face in $\{\mathcal{X}\}$, and implement *Surface Representation* to obtain the normalized LSDs that serve as the input of network. Then we compute the corresponding normalized noise-free normals $\tilde{\mathbf{n}}^*$ and the offset $\tilde{\mathbf{v}}^* - \tilde{\mathbf{v}}$ from $\{\mathcal{X}^*\}$ as the ground truth. To prevent overfitting, we apply random rotations and jittering to the LSDs and ground truth.

We train *SurfaceFormer* on a server equipped with two RTX3090 GPUs and an AMD Ryzen 5900X CPU for 10^5 iteration, optimized with the Adam algorithm ($\beta_1 = 0.9$, $\beta_2 = 0.999$, learning rate = 0.0001, batch size = 80). The loss function covers both the normal and vertex offset regressions, which are measured by the L_1 distance between outputs and ground truth:

$$L = \sum_{f_i \in P} \|\tilde{\mathbf{n}}_i^* - \tilde{\mathbf{n}}_i\|_1 + \alpha \sum_{f_i \in P} \|(\tilde{\mathbf{v}}_i^* - \tilde{\mathbf{v}}_i) - \Delta \tilde{\mathbf{v}}_i\|_1 \quad (14)$$

where α is the weight parameter to balance the two loss terms, we find that setting $\alpha = 1$ can produce satisfactory denoising results.

5 EXPERIMENTS

This section presents the outcomes and analysis from comprehensive comparative experiments and ablation studies, conducted to validate the effectiveness and superiority of our proposed method.

5.1 Training Dataset

We employ three commonly used datasets from CNR [14], and individually train *SurfaceFormer* on them:

- **Synthetic dataset.** The dataset contains 21 noise-free synthetic meshes, and they are corrupted by three level of Gaussian noise: 0.1, 0.2 and 0.3 deviations relative to the average edge length, resulting in a total of 63 noisy meshes. These are categorized into: *CAD* (18 meshes with sharp edges), *Smooth* (24 meshes with curved surface and plane), and *Feature* (21 meshes with rich details). This dataset contains 3.0 million faces.

- **Kinect V1 dataset.** The dataset are captured from four statues with both Microsoft Kinect v1 and a high accuracy scanner. The collection comprises *Big Girl* (24 meshes), *Cone* (12 meshes), *David* (23 meshes) and *Pyramid* (12 meshes). Meshes captured by Microsoft Kinect v1 serve as the noisy instances, while those from the high-accuracy scanner serve as the ground truth. This dataset contains 2.4 million faces.

- **Kinect V2 dataset.** Analogous in structure to the Kinect V1 dataset but utilizing Microsoft Kinect v2 for scanning, this set includes *Big Girl* (24 meshes), *Cone* (12 meshes), *David* (24 meshes), *Pyramid* (12 meshes). This dataset contains 0.9 million faces.

5.2 Testing Dataset

We conduct experimental on five datasets. The first three, released by [14], are built using the same methodology as their training counterparts, comprising Synthetic, Kinect V1, and Kinect V2 datasets. These datasets are equipped with ground truth meshes, enabling both objective and subjective comparison. We utilize the *SurfaceFormer* trained on the corresponding training set to obtain the best results. Additionally, to evaluate the generalization capabilities of the compared methods, we introduce a Real-scanned dataset from [9], [53], obtained from unknown scanners. Finally, to validate the performance of *SurfaceFormer* in practical applications, we choose four point clouds from different scanned datasets and utilize the Poisson surface reconstruction [54] to build noisy meshes as the Reconstructed dataset. These two datasets lack ground truth meshes and are subject to subjective evaluation only. The *SurfaceFormer* trained on the Synthetic dataset is applied to denoise these meshes.

The specifics of each test dataset are as follows:

- **Synthetic dataset:** *CAD* (42 meshes), *Smooth* (21 meshes) and *Feature* (24 meshes).
- **Kinect V1 datasets:** *Boy* (24 meshes), *Girl* (25 meshes), *Cone* (12 meshes) and *Pyramid* (12 meshes).
- **Kinect V2 datasets:** *Boy* (24 meshes), *Girl* (24 meshes), *Cone* (12 meshes) and *Pyramid* (12 meshes).
- **Real-scanned dataset:** *Angel* and *Eagle*.
- **Reconstructed dataset:** *Bed* from ScanObjectNN [55], a sparse object dataset; *ScrewNut* from Visionair [56], another object dataset scanned by different device; *Pillar* from sydney urban objects dataset [57], a outdoor LiDAR dataset; *Soldier* from 8iVFB v2 [58], a dense photo-realistic dynamic datasets.

5.3 Comparison Study

We evaluate the performance of *SurfaceFormer* against six state-of-the-art methods across all the test datasets. The compared methods can be divided into two categories based on their geometrical representation:

- **Methods using regular representation.** This group includes Cascaded normal regression (CNR) [14], Normalnet (NFN) [18] and NormalNet (NNT) [15]. These methods transform noisy meshes into regular representations and leverage CNN or MLP-based networks.
- **Methods using graph-based representation.** This group includes GCN-Denoiser (GCN) [16], GeoBi (GEO) [20] and ResGEM (RES) [44]. These methods utilize graph-based

Metric		E_a (Degree)							$E_v(10^{-1})$						
Method		CNR	NFN	NNT	GCN	GEO	RES	Ours	CNR	NFN	NNT	GCN	GEO	RES	Ours
Synthetic	CAD	3.71	5.00	3.46	3.29	2.99	2.50	2.05	0.52	0.79	0.60	0.58	0.55	0.46	0.34
	Smooth	3.08	3.22	3.06	2.62	2.73	2.43	2.18	0.47	0.56	0.53	0.40	0.48	0.44	0.33
	Feature	6.34	5.74	6.71	5.08	5.14	4.72	4.32	0.80	0.85	0.99	0.68	0.76	0.65	0.57
	Average	4.28	4.77	4.26	3.62	3.52	3.10	2.71	0.58	0.75	0.69	0.56	0.59	0.51	0.40
Kinect V1	Boy	8.48	9.11	8.52	8.28	7.73	6.63	6.54	5.47	5.64	5.42	5.37	4.58	4.31	3.71
	Cone	8.80	9.47	8.87	8.73	7.39	5.80	4.29	5.22	5.44	5.19	5.15	4.26	3.83	2.67
	Girl	11.45	11.94	11.43	11.13	10.73	9.32	8.39	5.77	5.96	5.73	5.61	4.77	4.53	3.75
	Pyramid	8.13	9.24	8.96	9.03	7.92	6.08	4.87	4.95	5.20	5.10	5.09	4.13	3.80	2.88
	Average	9.49	10.16	9.65	9.45	8.73	7.33	6.53	5.45	5.65	5.44	5.37	4.52	4.22	3.42
Kinect V2	Boy	7.95	8.33	7.80	7.43	7.84	6.66	5.69	5.27	5.26	5.19	5.10	4.21	3.74	2.65
	Cone	6.34	6.62	6.45	5.86	5.98	4.74	3.47	4.47	4.39	4.41	4.31	2.95	2.87	1.95
	Girl	9.36	10.04	9.31	8.96	9.18	8.11	7.47	4.06	4.16	4.00	3.96	3.18	3.10	2.74
	Pyramid	6.76	7.04	7.04	6.44	6.69	5.18	4.14	4.21	4.18	4.16	4.07	3.64	2.89	2.31
	Average	7.96	8.40	7.95	7.51	7.79	6.58	5.65	4.56	4.57	4.49	4.42	3.56	3.24	2.51

TABLE 1
The objective comparison of E_a and E_v , the best and second best results are marked in red and blue, respectively.

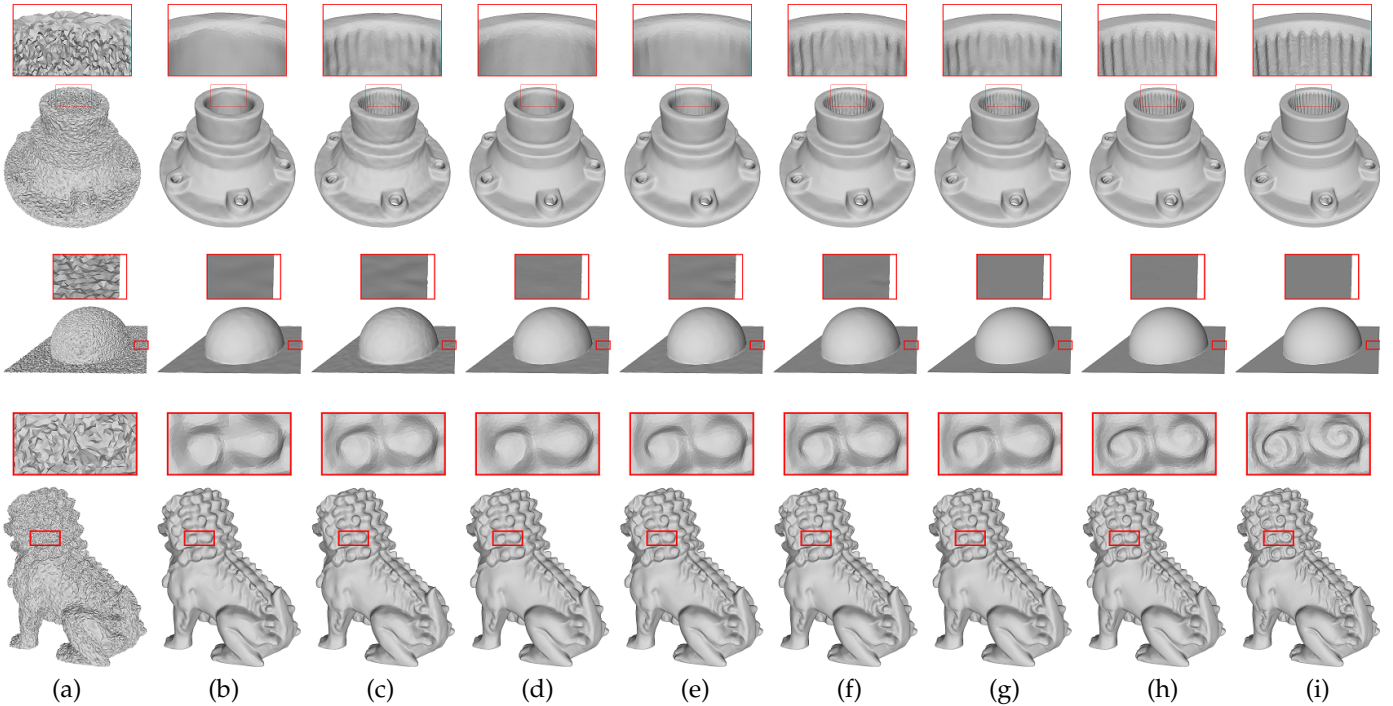


Fig. 7. Denoising results of CAD mesh *Carter100K*, Smooth mesh *Plane-sphere* and Feature mesh *Chinese-Lion* from synthetic dataset [14]. (a) the noisy meshes; (b) CNR [14]; (c) NFN [18]; (d) NNT [15]; (e) GCN [16]; (f) GEO [20]; (g) RES [44]; (h) Ours; (i) the ground truth.

representations to maintain the irregular structure of meshes and leverage GNN-based networks.

For CNR [14] and GCN [16], the authors kindly provided their code and pre-trained models of the three training datasets, allowing for direct application to the respective test datasets. For GEO [20], the authors provided the code and we strictly follow their paper to retrain the models on the training datasets. For NNT [15], NFN [18] and RES [44], the authors kindly provided us their denoised meshes for comparison.

5.4 Parameters Setting

For the iteration number in *Vertex Refinement*, we set $N_v = 60$. For the parameter in *Mesh Denoising*, we set the feature

dimension $D = 512$, the number of Transformer encoder $L = 12$, the number of heads $N_h = 12$. Following Vit [49], the MLP size is set to $4 \times D$. The choice of these parameters will be further discussed in *Ablation Study*.

For the parameters in *Patch Generation*, we set the face number of each patch $T_f = 240$, further increasing T_f will exceed the memory limitation of GPUs. For the parameters in *Surface Representation*, we set the precision of sampling $p_s = 8$, which aligns with the setting in prior work [15] for precise sampling. We set $T_s = 1.25 \times p_s$ to ensure the LSD contains 1-ring faces, which maintains adjacency relationships. The direction of normalization \mathbf{n}_t can be arbitrary and we set $\mathbf{n}_t = (1, 0, 0)$.

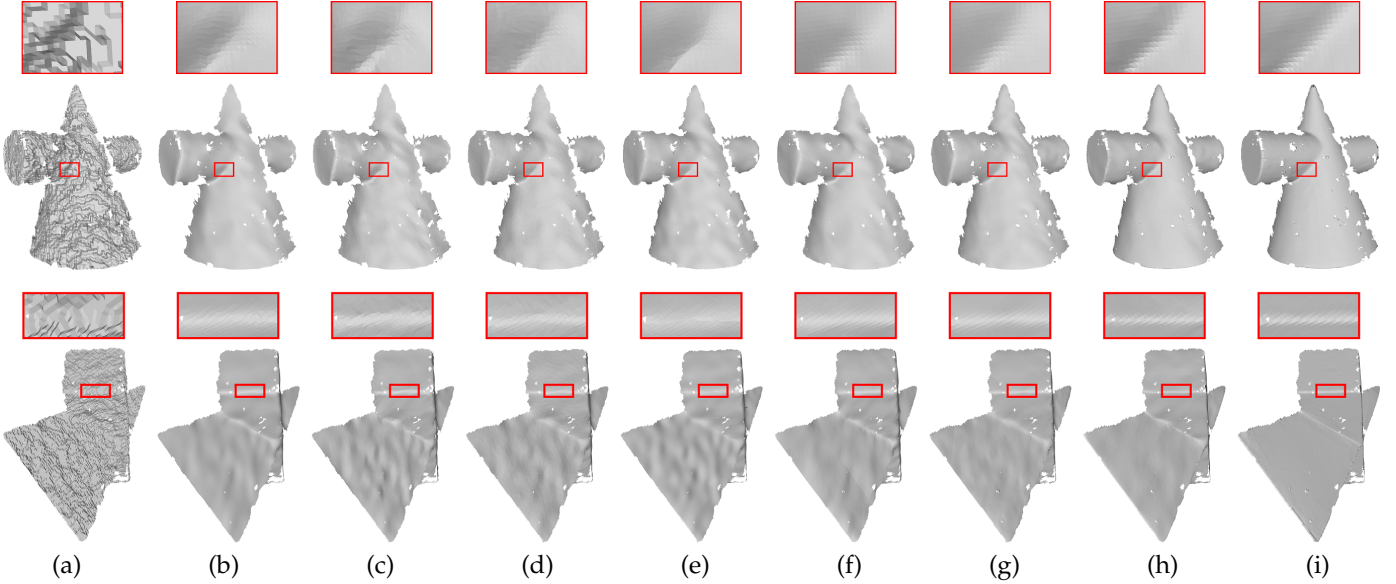


Fig. 8. Denoising results of *Cone_16* and *Pyramid_04* from Kinect V1 dataset [14]. (a) the noisy meshes; (b) CNR [14]; (c) NFN [18]; (d) NNT [15]; (e) GCN [16]; (f) GEO [20]; (g) RES [44]; (h) Ours; (i) the ground truth.

5.5 Objective Performance Comparison

– **Evaluation Metrics.** To assess our results and quantitatively contrast our method with the state-of-the-art methods, we employ two standard metrics, E_a and E_v , from GCN [16], which quantify errors in face normals and vertex positions, respectively. Specifically, E_a is the average normal angular difference between the denoised normals and ground truth:

$$E_a = \frac{1}{S_f} \sum_{i \in [1, S_f]} \text{acos}(\hat{\mathbf{n}}_i \cdot \mathbf{n}_i^*) \quad (15)$$

where S_f is total number of faces.

E_v is the normalized one-sided average Hausdorff distance from denoised vertices to the ground truth:

$$E_v = \frac{1}{S_v L_d} \sum_{\hat{\mathbf{v}}_i \in \hat{\mathbf{x}}} \min_{\mathbf{v}_j^* \in \mathbf{x}^*} \|\hat{\mathbf{v}}_i - \mathbf{v}_j^*\| \quad (16)$$

where S_v is total number of vertices, L_d is the average edge length of the ground truth mesh. Lower values of both metrics indicate higher quality.

– **Objective Comparison.** We present the comparison results of E_a and E_v in Table 1. For E_a , our method ranks first across all datasets, exhibiting average improvements of 12.6%, 10.9%, and 14.0% over the second-ranked method for each dataset, respectively. For E_v , our method also ranks first and achieves similar improvements on different dataset: 20.9%, 19.7%, and 22.5%, respectively. This demonstrates the effectiveness and robustness of our method in handling diverse noise types. Furthermore, due to the proposed LSD’s efficient preservation of local feature structures, our method demonstrates superior performance on meshes with significant features, such as the *CAD* category in the Synthetic dataset (E_a : 18.1%, E_v : 25.5%) and *Cone* category in the Kinect V1 dataset (E_a : 26.1%, E_v : 30.1%). This will be further demonstrated in the subsequent subjective comparison.

– **Time Efficiency.** We evaluated our method’s efficiency on the same server used for training. Statistically, generating

LSD operates at a rate of approximately 3980 LSDs per second on a single CPU core, and denoising operates at a rate of 144 patches per second on two GPUs. For better understanding, we take the Synthetic model *Child* as an example, which comprises 100K faces and is divided into 1208 patches. Our method requires only 25.12 seconds for LSD generation and 8.37 seconds for denoising. This performance is comparable with GCN [16], which takes 30 seconds to denoise *Child*. Furthermore, both LSD generation and denoising can be parallelized across multiple CPU cores and GPUs, respectively, potentially further reducing computation times.

5.6 Subjective Performance Comparison

– **Synthetic Dataset.** In Fig. 7, we present the visual comparison of *CAD* mesh *Carter100K*, *Smooth* mesh *Plane-sphere* and *Feature* mesh *Chinese-lion*. Our method outperforms others in both feature recovery and noise removal. Specifically, for *Carter100K* and *Chinese-lion*, the proposed LSD effectively retains rich mesh attributes, enabling precise differentiation of small-scale features from noise and leading to superior feature recovery. In contrast, other methods generally result in over-smoothing. For *Plane-sphere*, due to our method’s capability to aggregate global information, it successfully avoid mistaking local noise for feature structures, whereas other methods leave artifacts.

– **Kinect Dataset.** In Fig. 8, we illustrate the visual comparison of *Cone_16* and *Pyramid_04* from Kinect V1 Dataset. These meshes contains large-scale features with distributions distinct from synthetic meshes. Our method adeptly learns noise patterns to provide the best feature recovery for both meshes, while GCN [16], GEO [20] and RES [44] output over-smooth results, CNR [14], NFN [18] and NNT [15] struggle with noise removal, respectively. In Fig. 9, we show the visual comparison of *Girl_04* and *Boy_05* from Kinect V2 Dataset. These meshes contains rich detail and small-scale features. In *Girl_04*, only our method and RES [44] are able

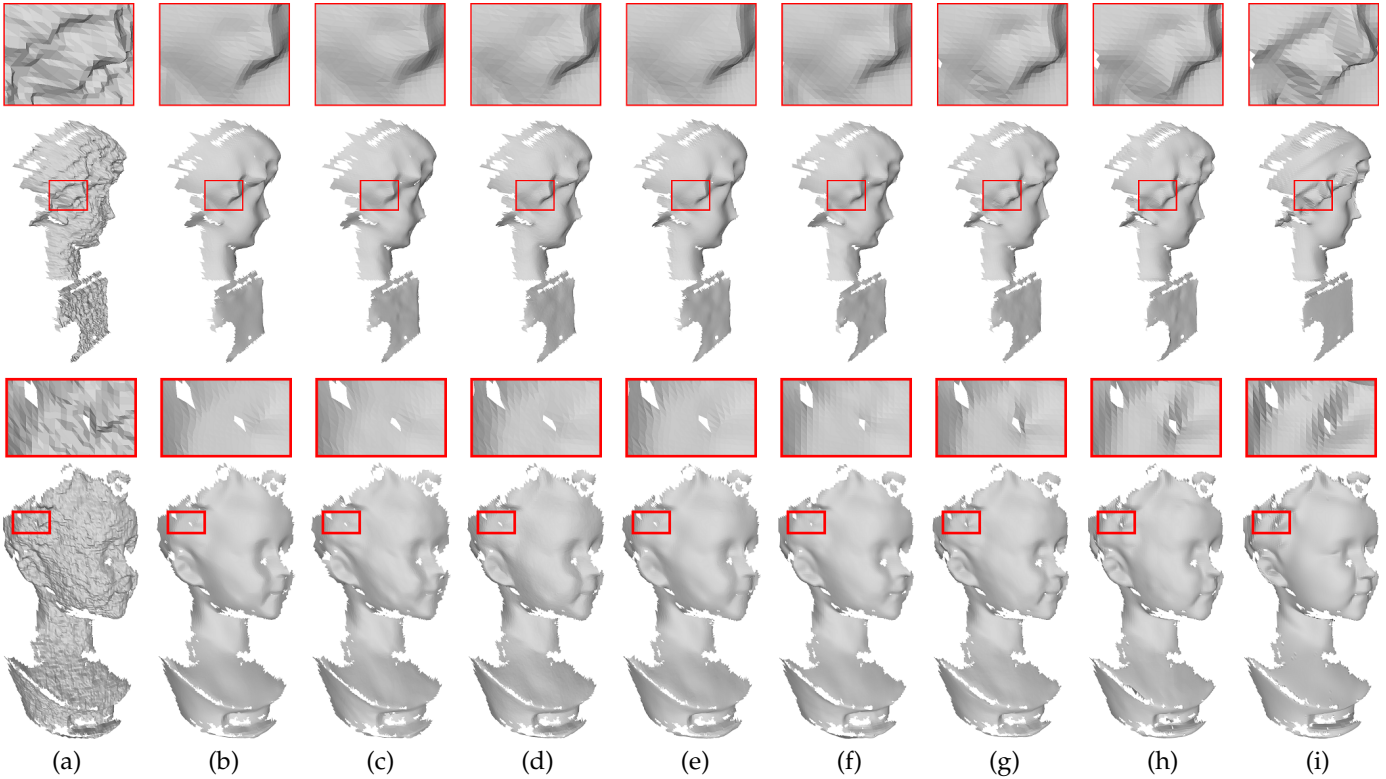


Fig. 9. Denoising results of *Girl_04* and *Boy_05* from Kinect V2 dataset [14]. (a) the noisy meshes; (b) CNR [14]; (c) NFN [18]; (d) NNT [15]; (e) GCN [16]; (f) GEO [20]; (g) RES [44]; (h) Ours; (i) the ground truth.

to preserve feature structures, but RES [44] fails to remove noise. In *Boy_05*, our method can preserve the feature while all the other methods introduce over-smoothing in the zoom-in region.

– **Real-Scanned Dataset.** To further assess our method’s robustness, in Fig. 10, we present the visual comparison of *Angel* and *Eagle*. Since that the authors of NFN [18] and RES [44] do not provide the results of these meshes, they are not included in this comparison. In *Angel*, CNR [14] and GEO [20] fail to catch the feature structures, resulting in over-smoothing outputs. NNT [15] and GCN [16] successfully perceive feature structures but cannot accurately restore the narrow edges. In contrast, our method produces the best feature recovery results. In *Eagle*, CNR [14], GCN [16] and GEO [20] can not remove noise, while NNT [15] can remove noise but introduces pseudo-feature. Our method accurately removes noise while restoring feature structures.

– **Reconstructed Dataset.** In real-world applications, a major resource for meshes stems from the reconstruction of point clouds. However, since acquired point clouds are typically sparse, the resulting meshes often suffer from reconstruction noise. In view of this issue, we evaluate the performance of *SurfaceFormer* on mitigating reconstruction noise. We present the denoising results in Fig. 11. Our method effectively manages different noise distributions from various scanners and achieves satisfactory feature recovery results in *ScrewNut* and *Pillar*. Moreover, our approach produces smooth surfaces in *Bed* and *Soldier*, avoiding the introduction of pseudo-features. This demonstrates that our algorithm accurately distinguishes features from noise in practical applications and achieves effective denoising.

Linear	Shape	Spatial	CAD	Smooth	Feature	Avg.
✓	×	×	2.11	2.33	4.57	2.84 (104%)
✓	✓	×	2.11	2.24	4.49	2.80 (102%)
✓	✓	✓	2.08	2.18	4.35	2.73 (100%)

TABLE 2
Ablation study on the Network structure.

Network	CAD	Smooth	Feature	Average.	Denoising Speed
<i>Small</i>	2.24	2.34	4.60	2.91 (107%)	161 LSD/s (112%)
<i>Middle</i>	2.08	2.18	4.35	2.73 (100%)	144 LSD/s (100%)
<i>Large</i>	2.01	2.07	4.31	2.66 (97%)	99 LSD/s (69%)

TABLE 3
Ablation study on the network parameters.

These experiments underscore our algorithm’s adeptness at restoring features across meshes produced by various scanning technologies.

5.7 Ablation Study

– **About the network structure.** To investigate the importance of various components of *SurfaceFormer*, we provide an ablation study to verify the effect of the Shape Embedding and Spatial Encoder on the Synthetic dataset. From Table 2, it can be observed that both the introduction of Shape Embedding and Spatial Encoder lead to a performance improvement on all categories, providing evidence of the effectiveness of our designed layers. Moreover, the introduction of spatial and edge information enhances the performance of distinguishing features: As shown in Fig. 12, the zoom-in region contains small-scale features, and the performance of

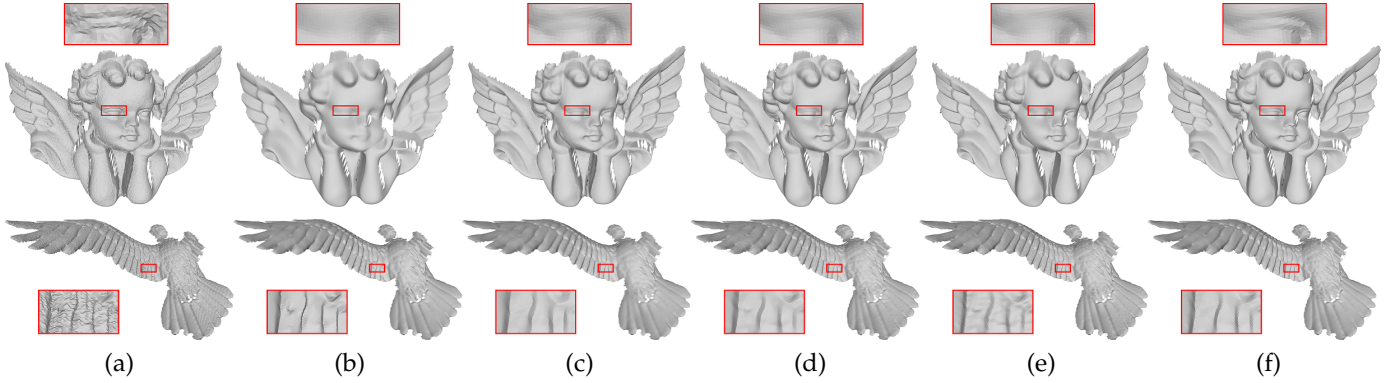


Fig. 10. Denoising results of *Angel* and *Eagle* from Real-scanned dataset [9], [53]. (a) the noisy meshes; (b) CNR [14]; (c) NNT [15]; (d) GCN [16]; (e) GEO [20]; (f) Ours.

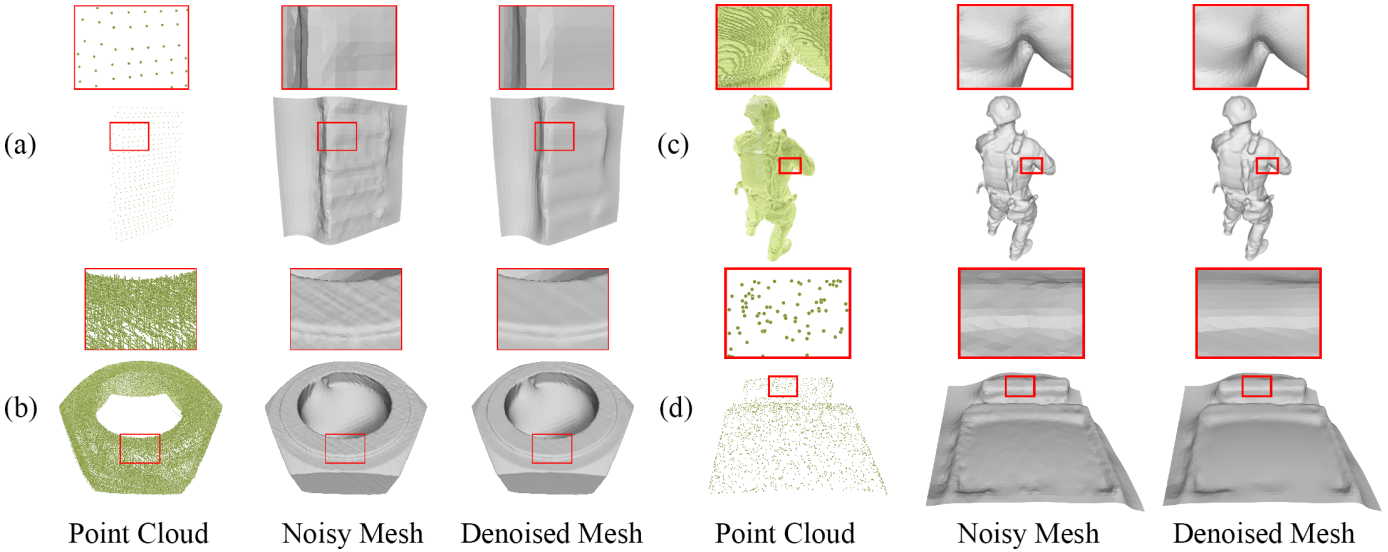


Fig. 11. Denoising results of Reconstructed dataset. (a) *Pillar* from sydney urban objects dataset [57]; (b) *ScrewNut* from Visionair [56]; (c) *Soldier* from 8iVFB v2 [58]; (d) *Bed* from ScanObjectNN [55].

feature recovering gradually improves with the introduction of these components.

– **About the multi-domain denoising.** Mesh denoising can be achieved in normal domain or vertex domain alone. However, integrating multi-domain information yields better results. To verify this, we apply *SurfaceFormer* to the *Boy_01* mesh from the Kinect V1 dataset, and obtain the denoised mesh through three methods: (1) normal domain denoising: employing the vertex updating method [9] to get denoised vertex according to the denoised normals; (2) vertex domain denoising: directly using the denoised vertex coordinates [29]; (3) multi-domain denoising: aligning the vertex coordinates to the normals as mentioned in *Vertex Refinement*. The denoising results are shown in Fig. 13. Specifically, method 1 can output smooth surface, but the distribution of vertices is corrupted by artificial effects. This is because the updating method [9] cannot catch the underlying distribution patterns of vertices. Method 2 can output vertices with a distribution similar to the ground truth. However, vertex coordinates exhibit less consistency compared to normals, resulting in rough surface. Method 3 integrates the consistency of normal and the distribution

vertex, leads to a satisfactory denoising effect.

– **About the choice of network parameter.** We conducted ablation study about three network parameters: the size of latent vector D , the number of Transformer encoders T and the number of attention heads N_h . To find the best combination of these parameters, we train three levels of networks with different parameters: *Small*: $D = 256, T = 8, N_h = 8$, *Middle* (Proposed): $D = 512, T = 12, N_h = 12$ and *Large*: $D = 1024, T = 16, N_h = 16$, then test them on the Synthetic dataset. As shown in Table 3, when the network parameters increase from *Small* to *Middle*, the denoising performance improves by 7% while the processing speed decreases by 12%. However, when the network parameters increase from *Middle* to *Large*, the performance only improves by 3% while the processing speed decreases by 31%. Considering the balance between speed and performance, we choose the *Middle* configuration ($D = 512, T = 12, N_h = 12$).

– **About the choice of N_v .** We provide ablation study about the iteration number N_v in *Vertex Refinement*. To determine the optimal choice of N_v , we perform *Vertex Refinement* on the Kinect V2 dataset, saving the denoised results after every 5 iterations, and then calculate the gain

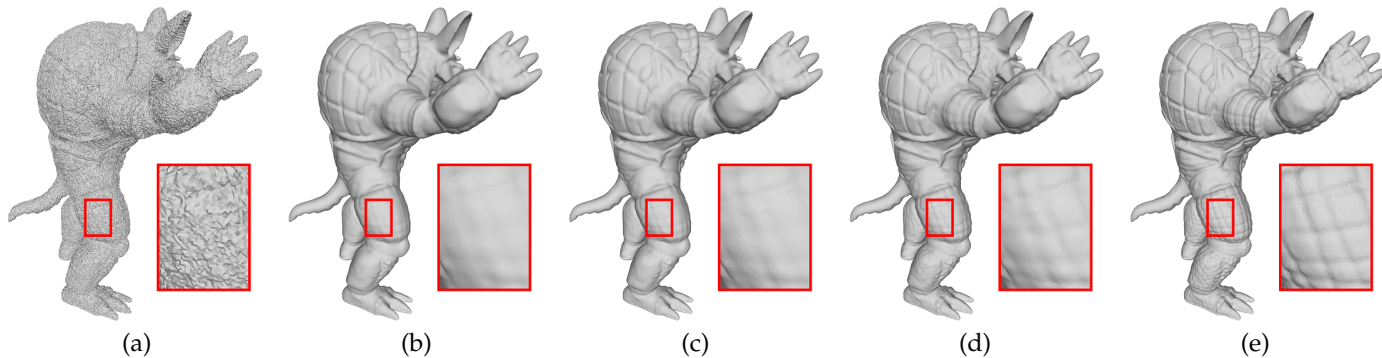


Fig. 12. Denoising results of *Feature* mesh *Armadillo* from synthetic dataset [14]. (a) the noisy meshes; (b) Linear embedding; (c) Linear embedding + shape embedding; (d) Full pipeline; (e) the ground truth.

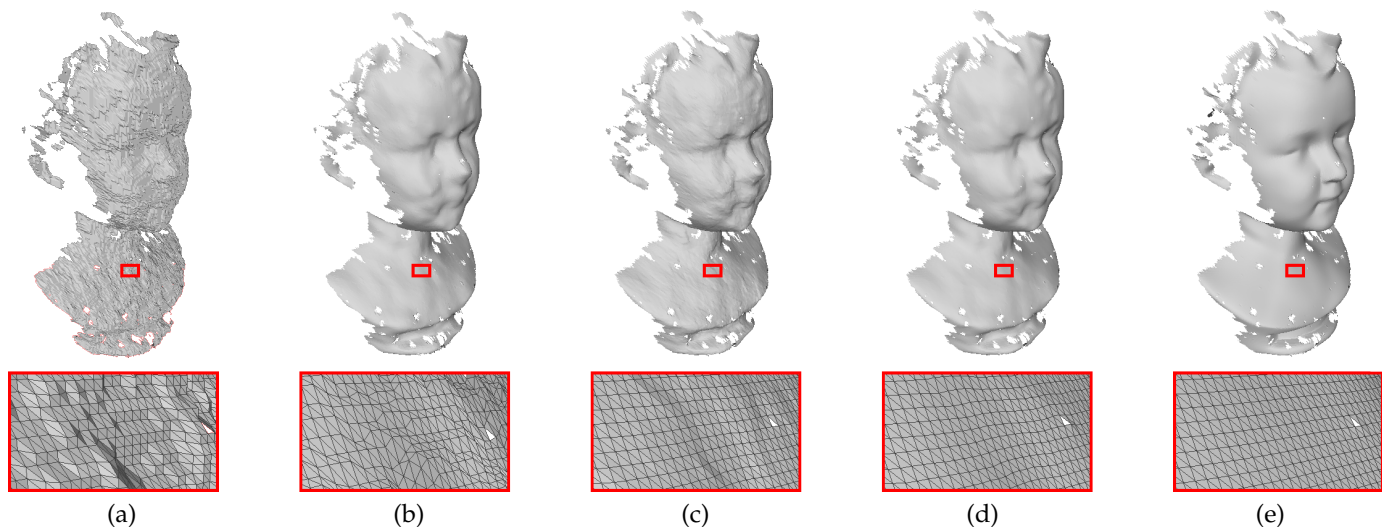


Fig. 13. Denoising results of mesh *Boy_01* from Kinect V1 dataset. (a) the noisy meshes; (b) denoising result in normal domain; (c) denoising result in vertex domain; (d) denoising result in multi domain; (e) the ground truth.

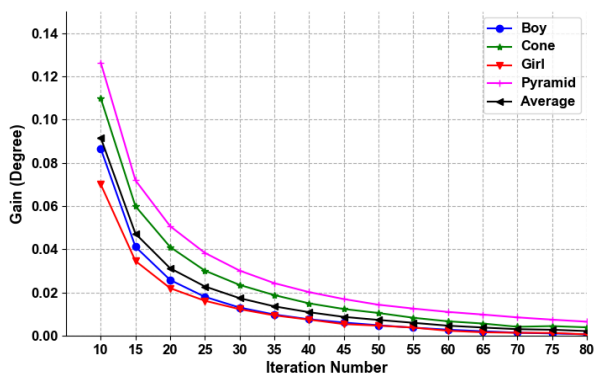


Fig. 14. The gain of E_a for every 5 iterations on Kinect V2 dataset.

of E_a between adjacent results. As shown in Fig. 14, the gain of each iteration decreases gradually as the iteration number increases. When the iteration number reaches 60, further increasing the iteration number would not result in a significant gain but only increase processing time. Therefore,

we choose $N_v = 60$.

6 CONCLUSION

Existing deep learning-based mesh denoising methods are constrained by single-modal geometric representations and network structures, limiting their capacity to capture the intricate attributes of meshes and accomplish effective global feature aggregation. In this paper, we introduced a novel and potent mesh denoising method, *SurfaceFormer*. Our first contribution is a novel multi-modal geometric representation called *Local Surface Descriptor* (LSD), which encodes local geometric details and spatial information into a sequence of 2D matrices and a point cloud, respectively. Next, we propose a dual-stream structure consisting of a Geometric Encoder branch and a Spatial Encoder branch, which jointly explore multimodal information for mesh denoising. A subsequent Denoising Transformer module receives the multimodal information and achieves efficient global feature aggregation through self-attention operators. Extensive experimental results demonstrate that our proposed method achieves superior performance in both objective and subjective evaluations compared to state-of-the-art mesh denoising techniques.

REFERENCES

- [1] Y. Mao, L. Wu, D.-M. Yan, J. Guo, C. W. Chen, and B. Chen, "Generating hybrid interior structure for 3d printing," *Computer Aided Geometric Design*, vol. 62, pp. 63–72, 2018.
- [2] M. Wei, L. Zhu, J. Yu, J. Wang, W.-M. Pang, J. Wu, J. Qin, and P.-A. Heng, "Morphology-preserving smoothing on polygonized isosurfaces of inhomogeneous binary volumes," *Computer-Aided Design*, vol. 58, pp. 92–98, 2015.
- [3] A. Hamidian, C. E. Palazzi, T. Y. Chong, M. Gerla *et al.*, "Exploring wireless mesh networks for collaborative augmented reality environments," *International Journal of Virtual Reality*, vol. 9, no. 2, pp. 21–30, 2010.
- [4] C. Tomasi and R. Manduchi, "Bilateral filtering for gray and color images," in *Sixth international conference on computer vision (IEEE Cat. No. 98CH36271)*. IEEE, 1998, pp. 839–846.
- [5] Z. Li, J. Zheng, Z. Zhu, W. Yao, and S. Wu, "Weighted guided image filtering," *IEEE Transactions on Image processing*, vol. 24, no. 1, pp. 120–129, 2014.
- [6] L. Xu, C. Lu, Y. Xu, and J. Jia, "Image smoothing via l0 gradient minimization," in *Proceedings of the 2011 SIGGRAPH Asia conference*, 2011, pp. 1–12.
- [7] M. Elad and M. Aharon, "Image denoising via sparse and redundant representations over learned dictionaries," *IEEE Transactions on Image processing*, vol. 15, no. 12, pp. 3736–3745, 2006.
- [8] Y. Zheng, H. Fu, O. K.-C. Au, and C.-L. Tai, "Bilateral normal filtering for mesh denoising," *IEEE Transactions on Visualization and Computer Graphics*, vol. 17, no. 10, pp. 1521–1530, 2011.
- [9] W. Zhang, B. Deng, J. Zhang, S. Bouaziz, and L. Liu, "Guided mesh normal filtering," in *Computer Graphics Forum*, vol. 34, no. 7. Wiley Online Library, 2015, pp. 23–34.
- [10] W. Zhao, X. Liu, S. Wang, X. Fan, and D. Zhao, "Graph-based feature-preserving mesh normal filtering," *IEEE Transactions on Visualization and Computer Graphics*, 2019.
- [11] L. He and S. Schaefer, "Mesh denoising via l0 minimization," *ACM Transactions on Graphics*, vol. 32, no. 4, p. 64, 2013.
- [12] X. Wu, J. Zheng, Y. Cai, and C.-W. Fu, "Mesh denoising using extended rof model with l1 fidelity," in *Computer Graphics Forum*, vol. 34, no. 7. Wiley Online Library, 2015, pp. 35–45.
- [13] Y. Zhao, H. Qin, X. Zeng, J. Xu, and J. Dong, "Robust and effective mesh denoising using l0 sparse regularization," *Computer-Aided Design*, vol. 101, pp. 82–97, 2018.
- [14] P.-S. Wang, Y. Liu, and X. Tong, "Mesh denoising via cascaded normal regression," *ACM Transactions on Graphics (SIGGRAPH Asia)*, vol. 35, no. 6, 2016.
- [15] W. Zhao, X. Liu, Y. Zhao, X. Fan, and D. Zhao, "Normalnet: learning-based mesh normal denoising via local partition normalization," *IEEE Transactions on Circuits and Systems for Video Technology*, vol. 31, no. 12, pp. 4697–4710, 2021.
- [16] Y. Shen, H. Fu, Z. Du, X. Chen, E. Burnaev, D. Zorin, K. Zhou, and Y. Zheng, "Gcn-denoiser: Mesh denoising with graph convolutional networks," *ACM Transactions on Graphics*, 2021.
- [17] J. Wang, J. Huang, F. L. Wang, M. Wei, H. Xie, and J. Qin, "Data-driven geometry-recovering mesh denoising," *Computer-Aided Design*, vol. 114, pp. 133–142, 2019.
- [18] Z. Li, Y. Zhang, Y. Feng, X. Xie, Q. Wang, M. Wei, and P.-A. Heng, "Normal-net: Normal filtering neural network for feature-preserving mesh denoising," *Computer-Aided Design*, p. 102861, 2020.
- [19] M. Armando, J.-S. Franco, and E. Boyer, "Mesh denoising with facet graph convolutions," *IEEE Transactions on Visualization and Computer Graphics*, 2020.
- [20] Y. Zhang, G. Shen, Q. Wang, Y. Qian, M. Wei, and J. Qin, "Geobignn: geometry-aware bi-domain mesh denoising via graph neural networks," *Computer-Aided Design*, vol. 144, p. 103154, 2022.
- [21] A. Vaswani, N. Shazeer, N. Parmar, J. Uszkoreit, L. Jones, A. N. Gomez, L. Kaiser, and I. Polosukhin, "Attention is all you need," *Advances in neural information processing systems*, vol. 30, 2017.
- [22] X. Wang, R. Girshick, A. Gupta, and K. He, "Non-local neural networks," in *Proceedings of the IEEE conference on computer vision and pattern recognition*, 2018, pp. 7794–7803.
- [23] X.-J. Li, J. Yang, and F.-L. Zhang, "Laplacian mesh transformer: Dual attention and topology aware network for 3d mesh classification and segmentation," in *European Conference on Computer Vision*. Springer, 2022, pp. 541–560.
- [24] H.-Y. Peng, M.-H. Guo, Z.-N. Liu, Y.-L. Yang, and T.-J. Mu, "Mw-former: Mesh understanding with window-based transformer," *Computers & Graphics*, vol. 115, pp. 382–391, 2023.
- [25] K. Lin, L. Wang, and Z. Liu, "Mesh graphormer," in *Proceedings of the IEEE/CVF international conference on computer vision*, 2021, pp. 12 939–12 948.
- [26] —, "End-to-end human pose and mesh reconstruction with transformers," in *Proceedings of the IEEE/CVF conference on computer vision and pattern recognition*, 2021, pp. 1954–1963.
- [27] K. Lin, C.-C. Lin, L. Liang, Z. Liu, and L. Wang, "Mpt: Mesh pre-training with transformers for human pose and mesh reconstruction," in *Proceedings of the IEEE/CVF Winter Conference on Applications of Computer Vision*, 2024, pp. 3415–3425.
- [28] W. Zhao, X. Liu, J. Jiang, D. Zhao, G. Li, and X. Ji, "Local surface descriptor for geometry and feature preserved mesh denoising," *Proceedings of the AAAI Conference on Artificial Intelligence*, vol. 36, no. 3, pp. 3446–3453, Jun. 2022. [Online]. Available: <https://ojs.aaai.org/index.php/AAAI/article/view/20255>
- [29] S. Fleishman, I. Drori, and D. Cohen-Or, "Bilateral mesh denoising," in *ACM Transactions on Graphics*, vol. 22, no. 3, 2003, pp. 950–953.
- [30] T. R. Jones, F. Durand, and M. Desbrun, "Non-iterative, feature-preserving mesh smoothing," in *ACM Transactions on Graphics*, vol. 22, no. 3, 2003, pp. 943–949.
- [31] U. Clarenz, U. Diewald, and M. Rumpf, *Anisotropic geometric diffusion in surface processing*. IEEE, 2000.
- [32] C. L. Bajaj and G. Xu, "Anisotropic diffusion of surfaces and functions on surfaces," *ACM Transactions on Graphics (TOG)*, vol. 22, no. 1, pp. 4–32, 2003.
- [33] M. Desbrun, M. Meyer, P. Schroder, and A. H. Barr, *Implicit Fairing of Irregular Meshes Using Diffusion and Curvature Flow*, 1st ed. New York, NY, USA: Association for Computing Machinery, 2023. [Online]. Available: <https://doi.org/10.1145/3596711.3596729>
- [34] W. Zhao, X. Liu, S. Wang, X. Fan, and D. Zhao, "Graph-based feature-preserving mesh normal filtering," *IEEE Transactions on Visualization and Computer Graphics*, vol. 27, no. 3, pp. 1937–1952, 2019.
- [35] W. Zhao, X. Liu, S. Wang, and D. Zhao, "Multi-scale similarity enhanced guided normal filtering," in *Advances in Multimedia Information Processing-PCM 2017: 18th Pacific-Rim Conference on Multimedia, Harbin, China, September 28-29, 2017, Revised Selected Papers, Part II 18*. Springer, 2018, pp. 645–653.
- [36] M. Wei, J. Huang, X. Xie, L. Liu, J. Wang, and J. Qin, "Mesh denoising guided by patch normal co-filtering via kernel low-rank recovery," *IEEE transactions on visualization and computer graphics*, vol. 25, no. 10, pp. 2910–2926, 2018.
- [37] M. Wei, X. Guo, J. Huang, H. Xie, H. Zong, R. Kwan, F. L. Wang, and J. Qin, "Mesh defiltering via cascaded geometry recovery," in *Computer Graphics Forum*, vol. 38, no. 7. Wiley Online Library, 2019, pp. 591–605.
- [38] X. Li, R. Li, L. Zhu, C.-W. Fu, and P.-A. Heng, "Dnf-net: a deep normal filtering network for mesh denoising," *IEEE Transactions on Visualization and Computer Graphics*, 2020.
- [39] D. Zhu, Y. Zhang, Z. Li, W. Wang, H. Xie, M. Wei, G. Cheng, and F. L. Wang, "Cascaded normal filtering neural network for geometry-aware mesh denoising of measurement surfaces," *IEEE Transactions on Instrumentation and Measurement*, vol. 70, pp. 1–13, 2021.
- [40] S. Hattori, T. Yatagawa, Y. Ohtake, and H. Suzuki, "Learning self-prior for mesh denoising using dual graph convolutional networks," in *European Conference on Computer Vision*. Springer, 2022, pp. 363–379.
- [41] W. Tang, Y. Gong, and G. Qiu, "Feature preserving 3d mesh denoising with a dense local graph neural network," *Computer Vision and Image Understanding*, vol. 233, p. 103710, 2023.
- [42] Z. Zhao, W. Wu, H. Liu, and Y. Gong, "A multi-stream network for mesh denoising via graph neural networks with gaussian curvature," in *2023 IEEE International Conference on Image Processing (ICIP)*. IEEE, 2023, pp. 1355–1359.
- [43] Z. Zhao, W. Tang, and Y. Gong, "Curvature-driven multi-stream network for feature-preserving mesh denoising," in *Computer Graphics Forum*, vol. 43, no. 1. Wiley Online Library, 2024, p. e14993.
- [44] Z. Zhou, M. Yuan, M. Zhao, J. Guo, and D.-M. Yan, "Resgem: Multi-scale graph embedding network for residual mesh denoising," *IEEE Transactions on Visualization and Computer Graphics*, 2024.
- [45] Q. Xie, Z. Dai, E. Hovy, T. Luong, and Q. Le, "Unsupervised data augmentation for consistency training," *Advances in neural information processing systems*, vol. 33, pp. 6256–6268, 2020.

- [46] M. Joshi, O. Levy, D. S. Weld, and L. Zettlemoyer, "Bert for coreference resolution: Baselines and analysis," *arXiv preprint arXiv:1908.09091*, 2019.
- [47] I. Kokkinos, M. M. Bronstein, R. Litman, and A. M. Bronstein, "Intrinsic shape context descriptors for deformable shapes," *2012 IEEE Conference on Computer Vision and Pattern Recognition*, pp. 159–166, 2012.
- [48] K. K. Liang, "Efficient conversion from rotating matrix to rotation axis and angle by extending rodrigues' formula," *arXiv preprint arXiv:1810.02999*, 2018.
- [49] A. Dosovitskiy, L. Beyer, A. Kolesnikov, D. Weissenborn, X. Zhai, T. Unterthiner, M. Dehghani, M. Minderer, G. Heigold, S. Gelly *et al.*, "An image is worth 16x16 words: Transformers for image recognition at scale," *arXiv preprint arXiv:2010.11929*, 2020.
- [50] K. He, X. Zhang, S. Ren, and J. Sun, "Deep residual learning for image recognition," in *IEEE Conference on Computer Vision and Pattern Recognition*, 2016, pp. 770–778.
- [51] H. Zhao, J. Jia, and V. Koltun, "Exploring self-attention for image recognition," in *Proceedings of the IEEE/CVF conference on computer vision and pattern recognition*, 2020, pp. 10 076–10 085.
- [52] Y. Wang, Y. Sun, Z. Liu, S. E. Sarma, M. M. Bronstein, and J. M. Solomon, "Dynamic graph cnn for learning on point clouds," *ACM Transactions on Graphics (tog)*, vol. 38, no. 5, pp. 1–12, 2019.
- [53] S. K. Yadav, U. Reitebuch, and K. Polthier, "Mesh denoising based on normal voting tensor and binary optimization," *IEEE Transactions on Visualization and Computer Graphics*, vol. 24, no. 8, pp. 2366–2379, Aug 2018.
- [54] M. Kazhdan and H. Hoppe, "Screened poisson surface reconstruction," *ACM Transactions on Graphics (ToG)*, vol. 32, no. 3, pp. 1–13, 2013.
- [55] M. A. Uy, Q.-H. Pham, B.-S. Hua, T. Nguyen, and S.-K. Yeung, "Revisiting point cloud classification: A new benchmark dataset and classification model on real-world data," in *CVPR*, 2019, pp. 1588–1597.
- [56] M. Attene, F. Giannini, M. Pitikakis, and M. Spagnuolo, "The visionair infrastructure capabilities to support research," *Computer-Aided Design and Applications*, vol. 10, no. 5, pp. 851–862, 2013.
- [57] M. De Deuge, A. Quadros, C. Hung, and B. Douillard, "Unsupervised feature learning for classification of outdoor 3d scans," in *Australasian conference on robotics and automation*, vol. 2, no. 1. University of New South Wales Kensington, Australia, 2013.
- [58] d. Eugene, H. Bob, M. Taos, and A. C. Philip, "8i voxelized full bodies - a voxelized point cloud dataset," in *ISO/IEC JTC1/SC29 Joint WG11/WG1 (MPEG/JPEG) input document WG11M40059/WG1M74006*, 2017.